

# On the Growth of Highly Ordered Pores in Anodized Aluminum Oxide

Feiyue Li,<sup>†</sup> Lan Zhang,<sup>‡</sup> and Robert M. Metzger\*

Center for Materials for Information Technology and Department of Chemistry, Box 870336,  
The University of Alabama, Tuscaloosa, Alabama 35487-0336

Received March 17, 1998. Revised Manuscript Received May 21, 1998

It is now established that hexagonally ordered domain structures can be formed in anodic alumina films by repeated anodization and stripping of the porous oxide. We find that the domain size is a linear function of time and increases with temperature. The pore density is initially high but decreases with anodizing time, as dominant pores deepen. Very small pores exist in native oxide in air or nucleate after electropolishing. Pore growth may start when the electric field increases at the pore bottoms, and acid dissolves the oxide locally.

## 1. Introduction

The protection or decoration of Al surfaces by anodization has been used commercially since at least 1923.<sup>1</sup> Self-organized “nanopore” structures in anodic alumina films, called “alumite”, have attracted great attention<sup>2–8</sup> due to their high pore density and their potential use for masking or information storage.<sup>5,9</sup> When the pores are filled with metals or semiconductors in a subsequent alternating-current reductive electrolysis, these films can be fabricated into interesting magnetic recording, electronic, and electrooptical devices.<sup>5,7,11–22</sup> These

“nanopores” can be used as templates for forming arrays of nanowires either embedded in alumite<sup>9,11,12,14,16–21</sup> or “freed” by a subsequent chemical removal of the alumite structure.<sup>7,23,24</sup>

Two forms of anodic aluminum oxide exist, the nonporous barrier oxide and the porous oxide. When Al is anodized in neutral or basic solutions (pH > 5), a flat, nonporous, featureless insulating “barrier” oxide forms,<sup>8</sup> the “barrier-type film” (BTF). When Al is anodized in an acid [usually sulfuric (H<sub>2</sub>SO<sub>4</sub>), oxalic (H<sub>2</sub>C<sub>2</sub>O<sub>4</sub>), or phosphoric (H<sub>3</sub>PO<sub>4</sub>) acids], deep pores can form,<sup>25</sup> with diameters varying between 5 and 100 nm and lengths up to several microns. The bottom of each pore also consists of a thin “barrier layer” (10–100 nm thick) over the metallic Al surface; the pore diameter depends on pH, anodization voltage, and choice of acid. This porous structure has been called “pore-type film” (PTF) or “alumite”.<sup>2,3,11</sup> The morphology of PTF is shown in Figure 1.<sup>26,27</sup>

Nonporous “barrier” oxides can form in several “valve metals”, i.e., in metals (Al, Bi, Sb, Ta) that act as diodes or rectifiers after the oxide layer has grown; some other metals have an incomplete “valve” effect (Ag, Cd, Fe, Mg, Si, Sn, W, Zn, and Zr).<sup>8</sup> Among the valve metals, pores are known to form in Al anodized in strong acids and in Si anodized in hydrofluoric acid,<sup>28–31</sup> but the

\* To whom inquiries should be addressed.

<sup>†</sup> Present address: Headway Technologies, 497 South Hillview Drive, Milpitas, CA 95035.

<sup>‡</sup> Present address: HMT Technology, 1055 Page Ave., Fremont, CA 94538.

(1) Bengough, G. D.; Stuart, J. M. Brit. Patent 223,994, 1923.

(2) Diggle, J. W.; Downie, T. C.; Goulding, C. W. *Chem. Rev.* **1969**, *69*, 365.

(3) Thompson, G. E.; Wood, G. C. Anodic Films on Aluminium. In *Treatise on Materials Science and Technology*, Vol. 23: *Corrosion: Aqueous Process and Passive Films*; Scully, J. C., Ed.; Academic Press Inc.: New York, 1983; Chapter 5, pp 205–329.

(4) Wernick, S.; Pinner, R.; Sheasby, P. G. Anodizing of Aluminium: General Notes and Theory. In *The Surface Treatment Finishing of Aluminium and Its Alloys*, 2nd ed.; Finishing Publications Ltd.: Teddington, Middlesex, UK, 1987; Vol. 1, Chapter 6, p 289.

(5) *Report of the Research Group for Functionalizing of Aluminum and its Surface Films*, Light Metal Educ. Found.: Osaka, Japan, June, 1988.

(6) Despic, A. Parkhutik, V. P. Electrochemistry of Aluminum in Aqueous Solutions and Physics of its Anodic Oxide. In *Modern Aspects of Electrochemistry*; Bokris, J. O'M., White, R. E., Conway, B. E., Eds.; Plenum Press: New York, 1989; Vol. 23, Chapter 6, p 401.

(7) Martin, C. R. *Chem. Mater.* **1996**, *8*, 1739.

(8) Lohrengel, M. M. *Mater. Sci. Eng.* **1993**, *R11*, 243

(9) AlMawlawi, D.; Coombs, N.; Moskovits, M. *J. Appl. Phys.* **1991**, *70*, 4421.

(10) Bandyopadhyay, S.; Miller, A. E.; Chang, H. C.; Banerjee, G.; Yuzhakov, V.; Yue, D.-F.; Ricker, R. E.; Eastman, J. A.; Baugher, E.; Chandrasekhar, M. *Nanotechnology* **1996**, *7*, 360.

(11) Tsuya, N.; Tokushima, T.; Wakui, Y.; Saito, Y.; Nakamura, H.; Hayano, S.; Furugori, A.; Tanaka, M. *IEEE Trans. Magn.* **1986**, *MAG-22*, 1140.

(12) Tsuya, N.; Tokushima, T.; Shiraki, M.; Umehara, Y.; Saito, Y.; Nakahara, H.; Harada, Y. *IEEE Trans. Magn.* **1988**, *MAG-24*, 1790.

(13) Kawai, S. *Proc. Electrochem. Soc. (Proc. Symp. Electrochem. Technol. Electron.)* **1988**, *88-23*, 389.

(14) Spratt, G. W. D.; Bissell, P. R.; Chantrell, R. W.; Wohlfarth, E. P. *J. Magn. Magn. Mater.* **1988**, *75*, 309.

(15) Saito, M.; Kirihara, M.; Taniguchi, T.; Miyagi, M. *Appl. Phys. Lett.* **1989**, *55*, 607.

(16) Lyberatos, A.; Chantrell, R. W.; Sterringa, E. R.; Lodder, J. C. *J. Appl. Phys.* **1991**, *70*, 4431.

(17) Samwel, E. O.; Bissell, P. R.; Lodder, J. C. *J. Appl. Phys.* **1993**, *73*, 1353.

(18) Bao, X.; Li, F.; Metzger, R. M. *J. Appl. Phys.* **1996**, *79*, 4869.

(19) Li, F.; Metzger, R. M. *J. Appl. Phys.* **1997**, *81*, 3806.

(20) Li, F.; Metzger, R. M.; Doyle, W. D. *IEEE Trans. Magn.* **1997**, *MAG-33*, 3715.

(21) Zhang, L.; Cho, H. S.; Li, F.; Metzger, R. M.; Doyle, W. D. *J. Mater. Sci. Lett.* **1998**, *17*, 291.

(22) Li, F., Ph.D. Dissertation, University of Alabama, 1998.

(23) Masuda, H.; Satoh, M. *Jpn. Appl. Phys.* **1996**, *35*, L126.

(24) Masuda, H.; Fukuda, K. *Science* **1995**, *268*, 1466.

(25) Setoh, S.; Miyata, A. *Sci. Pap. Inst. Phys. Chem. Res. (Tokyo)* **1932**, *19*, 237.

(26) Keller, F.; Hunter, M. S.; Robinson, D. L. *J. Electrochem. Soc.* **1953**, *100*, 411.

(27) O'Sullivan, J. P.; Wood, G. C. *Proc. R. Soc. London* **1970**, *A317*, 511.

(28) Uhler, A. *Bell Syst. Techn. J.* **1956**, *35*, 333.

(29) Turner, D. R. *J. Electrochem. Soc.* **1958**, *105*, 402.

(30) Lehmann, V.; Gösele, U. *Appl. Phys. Lett.* **1991**, *58*, 856.

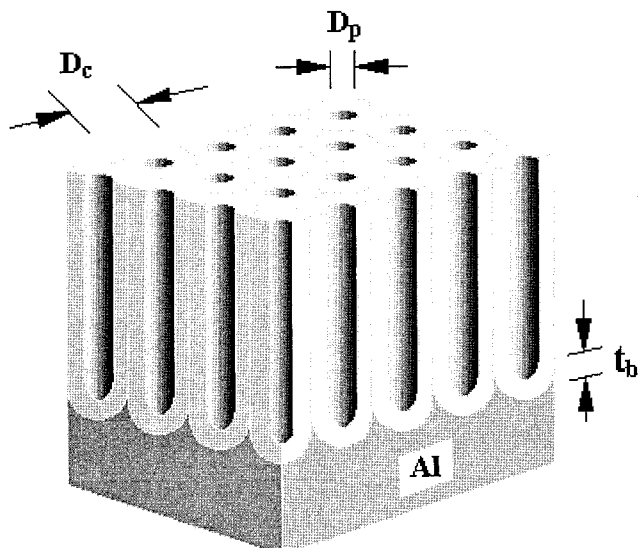


**Figure 1.** Ideal hexagonal "alumite", or PTF. Metallic Al, on the bottom, is covered by an impervious "barrier" oxide, of thickness  $d_b$ , and then by a hexagonal array of pores of diameter  $D_p$ , with a cell (repeat) distance  $D_c$ .<sup>26,27</sup>

mechanism for pore formation in Si, where the pores are wine-bottle shaped, is not understood.<sup>32</sup>

The PTF in Al form channels on the surface of the Al substrate. In the past 70 years, conventional anodization yielded only an approximately hexagonal arrangement of these pores. Several mechanisms for pore growth in Al PTF have been proposed.<sup>2-4,33,37</sup> Thompson, Wood, and co-workers proposed<sup>3</sup> that pore nucleation is due to a cracking and self-healing of the oxide layer atop preexisting ridges on the Al surface and that this forms a barrier layer of nonuniform thickness.<sup>2,34</sup>

Masuda and co-workers have grown an alumite film with a perfect hexagonal pore arrangement over a large area (micron scale),<sup>23,24</sup> by first anodizing Al for more than 10 h, dissolving alumina film, and then finally reanodizing for a few minutes. This has been repeated.<sup>21,35</sup> Recently Masuda and co-workers also formed a patterned SiC surface by electron beam lithography and used this pattern to "nanoindent" the Al surface at the "correct spacings" prior to anodization in acid, yielding a perfect hexagonal alumite pattern 2 mm  $\times$  2 mm.<sup>36</sup> Hexagonal ordering was also obtained during a high current density electropolishing step;<sup>10</sup> systematic variation of the electropolishing time and voltage established experimentally the regions of stability of hexagonal patterns, random patterns, and striped patterns.<sup>10</sup> A theoretical mechanism for hexagonal ordering was developed.<sup>37</sup>

(31) Parkhutiik, V. P.; Albella, J. M.; Martínez-Duart, J. M.; Gómez-Rodríguez, J. M.; Baró, A. M.; Shershulsky, V. I. *Appl. Phys. Lett.* **1993**, *62*, 366.

(32) Martínez-Duart, J. M.; Parkhutiik, V. P.; Guerrero-Lemus, R.; Moreno, J. D. *Adv. Mater.* **1995**, *7*, 226.

(33) Parkhutiik, V. P.; Shershulsky, V. I. *J. Phys.* **1992**, *D25*, 1258.

(34) Shimizu, K.; Kobayashi, K.; Thompson, G. E.; Wood, G. C. *Philos. Mag.* **1992**, *A66*, 643.

(35) Jessensky, O.; Müller, F.; Gösele, U. *Appl. Phys. Lett.* **1998**, *72*, 1173.

(36) Masuda, H.; Yamada, H.; Satoh, M.; Asoh, H.; Nako, M.; Tamura, T. *Appl. Phys. Lett.* **1997**, *71*, 2770.

(37) Yuzhakov, V. V.; Chang, H.-C.; Miller, A. E. *Phys. Rev.* **1997**, *B56*, 12608.

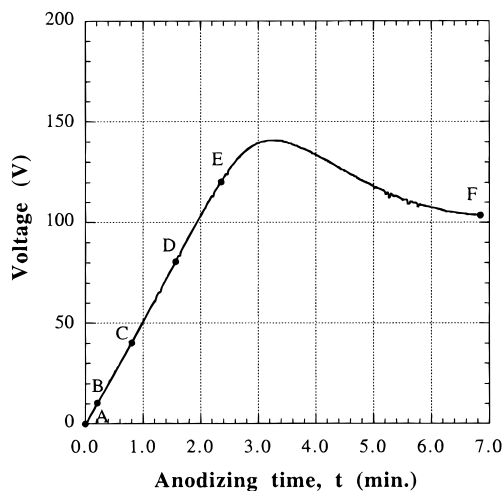


**Figure 2.** Voltage–time (V–t) anodization curve for anodization of an Al sheet in 4%  $\text{H}_3\text{PO}_4$  at a current density of 5  $\text{mA cm}^{-2}$  at room temperature. Round circles with labels (A,  $t = 0$  s; B,  $t = 10$  s; C,  $t = 50$  s; D,  $t = 100$  s; E,  $t = 150$  s; and F,  $t = 420$  s) correlate with the AFM images shown in Figure 3.

We studied the preparation<sup>18</sup> and magnetization decay of  $\alpha$ -Fe nanowires electroplated in alumite<sup>19,20</sup> and confirmed the formation of highly ordered pores.<sup>21</sup> In sections 2 and 3 we present new experimental observations about pore nucleation and growth. Section 4 reviews the phenomenological theories of pore formation, while section 5 presents mathematical theories of pore formation. Section 6 critically compares growth of BTF and PTF. In section 7 we discuss the chemistry and our own ideas for a mechanism for pore growth.

## 2. Experimental Section

**2.1. Al Surface Pretreatments.** An Al sheet [99.997% pure, Alfa, with (100) orientation] was first degreased in 5% NaOH at 60 °C for 30 s, rinsed with deionized water, neutralized in 1:1 water/ $\text{HNO}_3$  for several seconds, and then rinsed again with deionized water. The sample was electropolished in perchloric acid–ethanol solution (165 mL 65%  $\text{HClO}_4$ , 700 mL of ethanol, 100 mL of 2-butoxyethanol ("butyl cellulose"), and 137 mL of  $\text{H}_2\text{O}$ ) at a current density  $> 500$   $\text{mA cm}^{-2}$  for 1 min at  $< 10$  °C. After electropolishing, the sample was washed with warm deionized water and then rinsed in cold deionized water.

**2.2. Anodization.** Since the pore size is larger, but the pore growth rate is slower in  $\text{H}_3\text{PO}_4$  than in  $\text{H}_2\text{C}_2\text{O}_4$ ,<sup>3</sup> we chose  $\text{H}_3\text{PO}_4$  for pore nucleation studies and  $\text{H}_2\text{C}_2\text{O}_4$  for the pore growth studies.

In the pore nucleation studies, the pretreated Al samples were anodized at a constant current density of 5  $\text{mA cm}^{-2}$  (Fluke Model 341A) in 4%  $\text{H}_3\text{PO}_4$  at room temperature for a short time, using an Al counter electrode. The anodic alumina films were dissolved in a mixed solution of 0.2 M  $\text{H}_2\text{CrO}_4$  and 0.4 M  $\text{H}_3\text{PO}_4$  for 15 min at 60 °C.

For the studies of pore ordering, anodization was performed at 40 V dc in 3%  $\text{H}_2\text{C}_2\text{O}_4$  (Aldrich) at either 0 or 15 °C, in a constant-temperature bath (Fisher Isotemp 1016D). We modified Masuda and Fukuda's process,<sup>23,24</sup> as follows: (1) anodized a polished Al sheet for 5–10 min to eliminate large ridges and to "texture" the Al surface; (2) dissolved away the oxide film in a mixed solution of 0.2 M  $\text{H}_2\text{CrO}_4$  and 0.4 M  $\text{H}_3\text{PO}_4$  at 60 °C for, typically, 5 min; (3) anodized for 0.5–12 h, to create long-range ordering; (4) removed oxide film (optionally, repeated steps 3 and 4); and (5) anodized Al again under the same conditions, but only for 3 min. In step 5 the Al sheet becomes a template for growing highly ordered pores.<sup>23,24</sup>

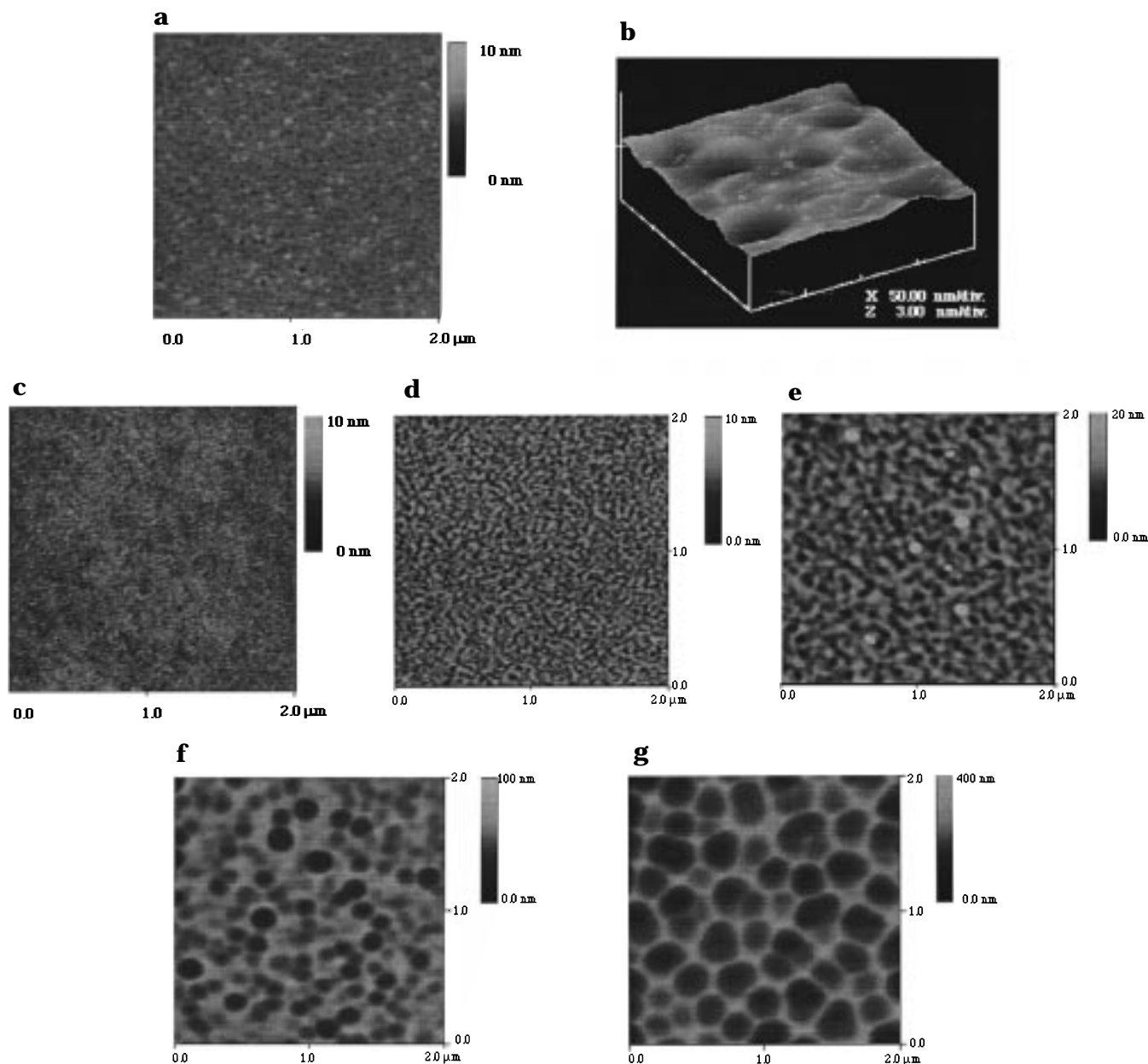


**Figure 3.** AFM tapping mode images of the Al surface in air after constant-current anodization ( $5 \text{ mA cm}^{-2}$ ) for time  $t$  and then stripping away of the PTF with phosphoric–chromic acids, corresponding to labeled points in Figure 2: (a) as-electropolished,  $t = 0$ , point A, “textured surface” of area  $2 \mu\text{m} \times 2 \mu\text{m}$ , vertical range 10 nm; (b) zoomed-in higher magnification image ( $0.2 \mu\text{m} \times 0.2 \mu\text{m}$ , vertical range 3 nm) of Figure 3a; (c) anodized for  $t = 10 \text{ s}$ , point B, area  $2 \mu\text{m} \times 2 \mu\text{m}$ , vertical range 10 nm; (d)  $t = 50 \text{ s}$ , point C, area  $2 \mu\text{m} \times 2 \mu\text{m}$ , vertical range 10 nm; (e)  $t = 100 \text{ s}$ , point D, area  $2 \mu\text{m} \times 2 \mu\text{m}$ , vertical range 100 nm; (f)  $t = 150 \text{ s}$ , point E, area  $2 \mu\text{m} \times 2 \mu\text{m}$ , vertical range 100 nm; (g)  $t = 420 \text{ s}$ , point E, area  $2 \mu\text{m} \times 2 \mu\text{m}$ , vertical range 400 nm.

### 2.3. Characterization of the Alumite Film Surface.

The surfaces of both the top of the anodic alumina films and of the precurved Al surface, after removal of the anodic alumina films, were studied by scanning electron microscopy (SEM, Philips XL30), by transmission electron microscopy (TEM, Hitachi H-8000), and by atomic force microscopy (AFM, Digital Instruments Nanoscope III and Dimension 3000).

**2.4. Stoichiometry of Film Growth.** An experiment was conducted to determine what percentage of the current is used to form oxide and what percentage of the current places Al ions into solution.

An Al sheet was anodized at 40 V and  $15^\circ\text{C}$  for 20 min in 3%  $\text{H}_2\text{C}_2\text{O}_4$ . The volume of the electrolyte was 150 mL. The Al sample was weighed on a Mettler microbalance before anodization, after anodization, and after stripping the alumite film. The electrical charge used in anodization was measured by integrating the current versus time chart (weighing the paper for the cut-out area under the curve). The porosity of

the alumite film was estimated from the pore structures measured by AFM, SEM, and TEM.

## 3. Results and Discussion

**3.1. Pore Nucleation.** An anodizing curve in 4%  $\text{H}_3\text{PO}_4$  at a constant current density of  $5 \text{ mA cm}^{-2}$  is shown in Figure 2. Initially ( $t = 0$ –2.5 min), the anodizing voltage increases linearly with time, implying a linear increase in resistance or a linear growth of high-resistance oxide, then the rate slows, and a local maximum appears ( $t = 3.2 \text{ min}$  in Figure 2). This behavior has been noted before.<sup>34</sup> In the initial period ( $t = 0$ –2.5 min) the resistance ( $R$ ) changes linearly with time; this implies an overall uniform growth of a film with constant resistivity.

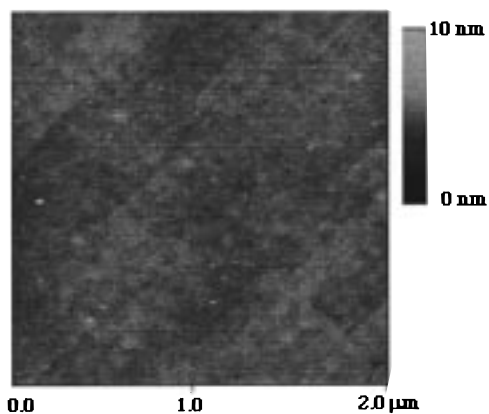


**Figure 4.** AFM tapping mode image ( $2\ \mu\text{m} \times 2\ \mu\text{m}$ ) of Al surface after anodization up to 60 V in 0.4%  $\text{H}_3\text{PO}_4$  at a constant current density of  $5\ \text{mA cm}^{-2}$  at room temperature

Figure 3a is an image of the electropolished Al surface before anodization. After electropolishing in perchloric acid–ethanol solution, Al has an almost flat surface, exhibiting small etch pits and bumps, which could be seeds for pore nucleation.

Figure 3c–g demonstrates pore nucleation and development on the anodic aluminum surface. Figure 3c shows that the pore nucleation occurs at the very beginning ( $t = 10\ \text{s}$ ). It suggests that the either nucleation has already occurred during electropolishing or that nucleation takes place almost at the same time as the barrier layer growth. At this point, the surface shows many small parallel grooves at low magnification, as shown in Figure 3c.

The initial pore density is very high, on the order of  $10^{10}$ – $10^{12}\ \text{cm}^{-2}$  (Figure 3b). Figure 3c–g shows that with increasing time, the pore size increases, but the pore density decreases: the pore increases in size by merging with adjacent pores.

Pore growth may be due to a field-assisted hydrogen ion attack on the oxide layer. If the hydrogen ion concentration is decreased, then this attack will be slow or stop and a BTF layer will form instead.<sup>34</sup> Indeed, Figure 4 shows an AFM image of an Al surface after anodization up to 60 V, under the same conditions as shown in Figure 3, but the  $\text{H}_3\text{PO}_4$  acid electrolyte was diluted 10 times, to 0.4%  $\text{H}_3\text{PO}_4$ . As compared to Figure 3d (up to 40 V), the Al surface is very flat and almost pore-free. So the hydrogen ion attack must be fundamental to pore nucleation and development.

The pore-type anodic aluminum oxide film grows in acidic solution, due to an electric-field-assisted local chemical dissolution at the oxide/electrolyte interface. Obviously, this local dissolution affects the surface features. Since the chemical dissolution is exothermic, the heat produced may cause a localized temperature increase.

**3.2. Highly Ordered Pore Growth.** The pore-type alumina films can be grown by anodizing Al at constant current or constant voltage. For growing the films with a desired pore diameter, the constant voltage mode is usually employed. Figures 5 and 6 show the anodization curves ( $j$ – $t$  and  $V$ – $t$ ) of a “textured” Al sheet at constant voltage of 40 V in 3%  $\text{H}_2\text{C}_2\text{O}_4$  at 15 °C. The solid line shows the first-time anodization curve; the dotted line shows the second-time anodization (after

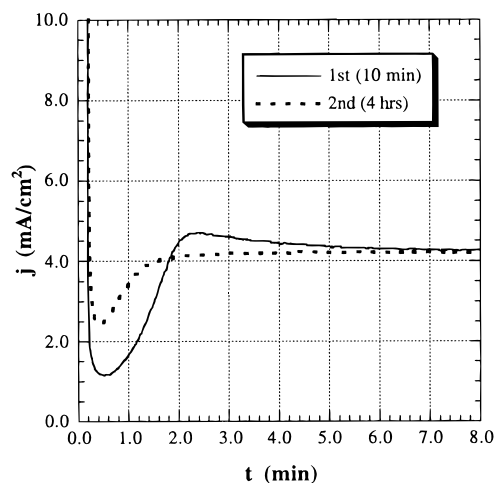


**Figure 5.** Current–time anodization curve ( $j$ – $t$ ) for anodization in 3%  $\text{H}_2\text{C}_2\text{O}_4$  at 40 V and 15 °C (constant-voltage mode).

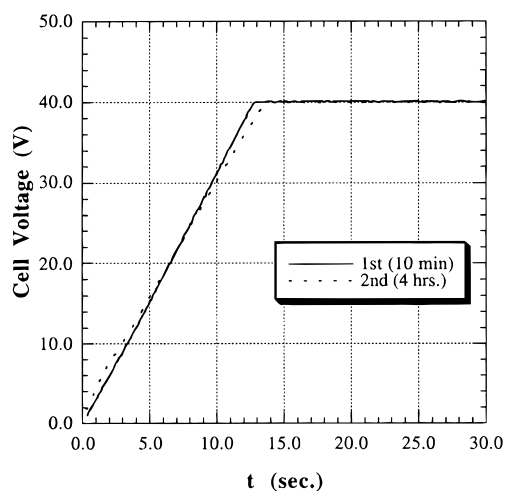


**Figure 6.** Voltage–time anodization curve ( $V$ – $t$ ) in 3%  $\text{H}_2\text{C}_2\text{O}_4$  at 15 °C. The constant-voltage mode is reached after 12–13 s.

stripping of the oxide and formation of a “textured surface”<sup>23,24</sup>).

The alumina film grows differently on the flat Al sheet (first anodization) than on the textured surface (second anodization). First, the minimum  $j$  is larger for the “textured” Al sheet than for the flat Al sheet. Next, there is no current overshoot for the “textured” Al sheet. Last, in Figure 6 the voltage increases more slowly with time ( $t = 0$ –12 s) for the second anodization than for the first anodization (the difference is reproducible, but barely above the error of measurement).

Since the textured surface shows a slightly slower increase of the voltage than the flat Al sheet, the alumina layer formed in air may be nonuniform. The thinnest oxide layer is probably at the bottom of each curvature, where the resistance is lowest and electric field is the highest. So the pore nucleation is easier on a “textured” surface, which results in a lower barrier layer growth rate. For the same reason, the pore growth current increases earlier for the textured surface sample. Therefore, for the textured surface sample the minimum current density is higher and there is no “overshoot” in Figure 5.

**3.3. SEM Images of Ordered Pores.** A perfect hexagonal arrangement of the pores was obtained when

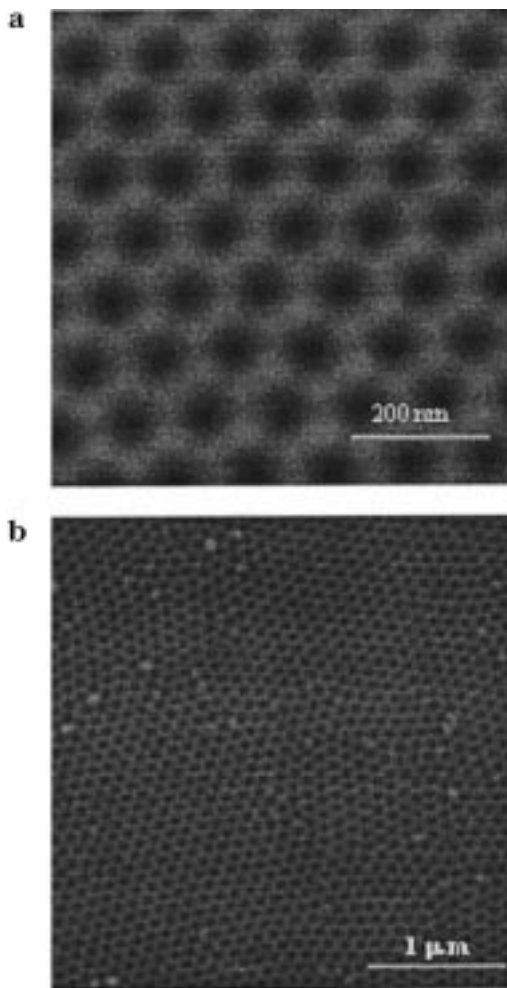


**Figure 7.** SEM images of anodic alumina films anodized at 40 V in 3%  $\text{H}_2\text{C}_2\text{O}_4$  at 15 °C three times: for 10 min, then 11.5 h, and then 3 min (the oxide is stripped away after the first and second anodizations): (a) high magnification, (b) low magnification.

anodization was conducted for a long time. Figure 7 shows the SEM images obtained after a first anodization of 10 min, a second anodization of 11.5 h, and a third anodization of 3 min (the oxide was stripped away after the first and second anodizations). At low magnification (Figure 7b), this ordered structure shows domain structures with an average size of about  $4 \mu\text{m}^2$ .

The domain structures should be a function of time. That means the domain can grow during anodization (Figures 9 and 10). At least two kinds of defects were found in the domains, such as point defects and misfit dislocations (Figure 9). There were some large "islands" (point defects), in the domain; each "island" was surrounded by more than three pores. On the other hand, the misfit dislocation of the pores line also interrupted the periodic arrangement of the pores (Figure 9).

The domain boundaries are also shown in Figure 10: the pores gradually merged along the boundaries. Maybe the bottoms of the pores could move around, and the domains grew by alignments and mergers of pores at domain boundaries, i.e., the domain size was a function of time. The domain areas were determined by first outlining the boundaries of several domains on SEM micrographs, counting the number of pores for several domains, converting these numbers to areas,

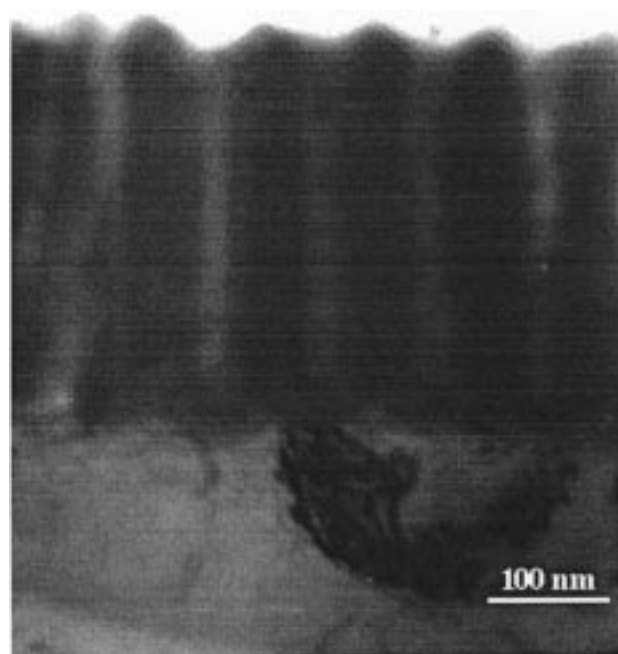


**Figure 8.** Cross-sectional TEM micrograph of alumite and Al metal bottom.

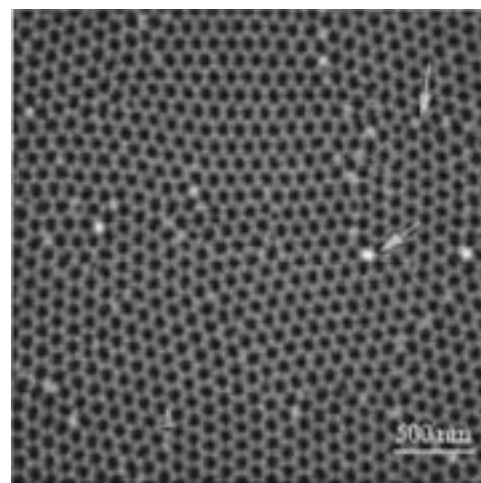


**Figure 9.** SEM image showing defects in the domain structures; the small arrows indicate point defects. Lattice mismatches can also be seen.

and averaging. The average domain area was a linear function of the time (Figure 11): this is very similar to grain growth in metals and alloys. For metals and alloys, the driving force of grain growth is the grain boundary energy per unit area. For grain growth at a fixed temperature, the average radius  $R$  of the grain is a function of the time  $t$ :

$$R = Bt^n \quad (1)$$

where  $B$  is a temperature-dependent parameter and  $n$  is about 0.5–0.4.<sup>38</sup>

This empirical equation is also suitable for domain growth in anodic alumina films (Figure 11). As the pores moved and merged, the orientation of adjacent

(38) Tu, K.; Mayer, J. W.; Feldman, L. C. *Electronic Thin Film Science for Electrical Engineers and Materials Scientists*; Macmillan Publishing Comp.: New York, 1992; p 370.

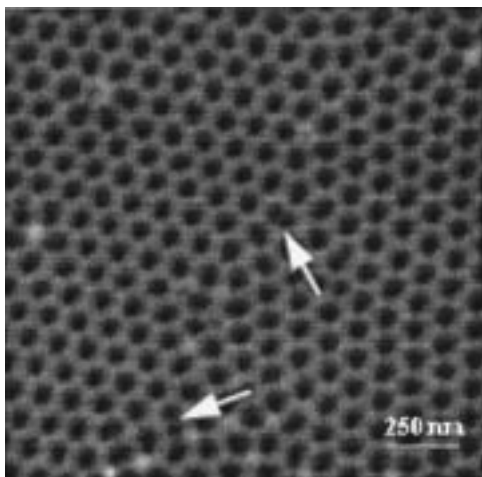


**Figure 10.** Domain boundaries and pore merging along the domain boundaries. The arrows show the merging of pores.

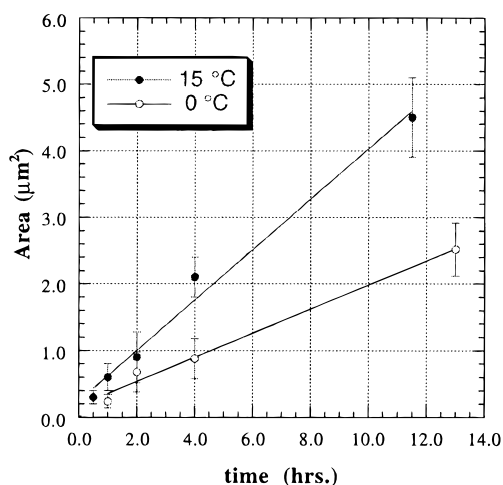


**Figure 11.** Domain growth as a function of anodizing time at 40 V in 3%  $\text{H}_2\text{C}_2\text{O}_4$ .

domains could change gradually, so domains smoothly matched each other.

**3.4. AFM Images of Ordered Pores.** The best way to understand pore growth would be to look at the oxide/electrolyte interface, but no nondestructive method can do this in air at the present time. The metal/oxide interface is close to the oxide/electrolyte interface and may be sensitive to changes at the oxide/electrolyte interface, i.e., at the other side of the barrier oxide layer. SEM images of the top of the surface cannot probe directly the bottom of the pores. One can remove the amorphous oxide growth and “peer below” it by AFM.

Figure 12a shows the top of anodic oxide film after reanodizing, for the same sample as shown in Figure 7: the AFM pattern was the same as seen by SEM. Figure 12b shows the AFM image after removing the anodic oxide film: now we see the bottom of the pores (plus any oxide grown from exposure to air). Again we see the familiar, highly ordered, hexagonal pattern.

The cross-sectional analysis of the AFM image (Figure 13) shows that the Al surface is curved, with a radius of curvature of about 60–65 nm. The interesting feature in Figures 12b and 13 is that each pore (or “scallop”) of about 100 nm diameter and 28 nm depth is surrounded by six “bumps” of about 20 nm diameter and about 10–13 nm height. The lack of circular

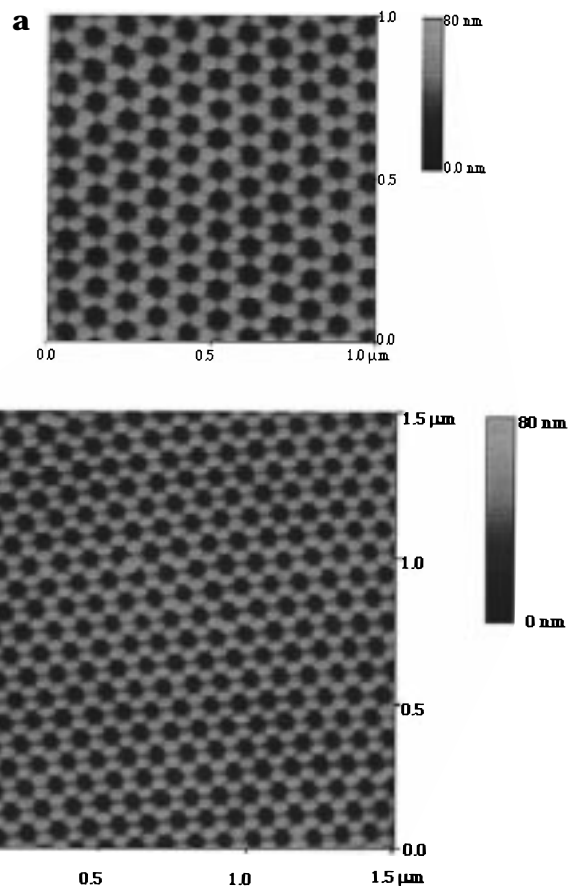


**Figure 12.** AFM images of (a) surface of anodic alumina film grown at 40 V in 3%  $\text{H}_2\text{C}_2\text{O}_4$  at 15 °C (oxide thickness about 300 nm) ( $1 \mu\text{m} \times 1 \mu\text{m}$ , vertical scale 80 nm) and (b) surface of Al substrate after the 300 nm thick anodic alumina film was stripped away with  $\text{H}_3\text{PO}_4$  and  $\text{H}_2\text{CrO}_4$  ( $1.5 \mu\text{m} \times 1.5 \mu\text{m}$ , vertical scale 80 nm).

symmetry of the aluminum oxide around each scallop and the presence of six “bumps” has not been reported before. Each scallop is surrounded by six bumps, and each bump is surrounded by three scallops. Also, there is a groove or “pass” between nearest neighbor bumps.

**3.5. Stoichiometry of Film Growth.** We found that during anodization in 3%  $\text{H}_2\text{C}_2\text{O}_4$  acid at 40 V, about 30% of the aluminum is dissolved into the electrolyte.

An Al sample was weighed before anodization ( $317\,769 \pm 2 \mu\text{g}$ ), after anodization ( $318\,191 \pm 2 \mu\text{g}$ ), and after stripping the alumite film ( $316\,440 \pm 2 \mu\text{g}$ ). The electrical charge transferred during anodization, 14.4 C, was obtained by integrating the area under the current versus time curve. This charge converted 1329 mg of Al into 1751 mg of  $\text{Al}_2\text{O}_3$  with a current efficiency of  $100 \times [14.4 \text{ C} \times 26.98 \text{ g mol}^{-1} / (3 \text{ electrons (Al atom)}^{-1} \times 96\,485 \text{ C mol}^{-1}) / 0.001\,329 \text{ g}] = 99.3\%$ . The percent yield of anhydrous  $\text{Al}_2\text{O}_3$  was  $(100 \times 0.001\,751 \times 26.98) / [0.001\,329 \times (0.5 \times 26.98 + 1.5 \times 15.9994)] = 69.73\%$ . This yield was also estimated by calculating the film porosity. From the measured pore diameter  $D_p = 60 \text{ nm}$ , cell size  $D_c = 104 \text{ nm}$  (minimum pore-to-pore distance), and pore density  $d = 1.118 \times 10^{10} \text{ pores cm}^{-2}$ , the porosity  $r = (\text{area of pores}) / (\text{film area}) = \pi(D_p/2)^2 \times 1.118 \times 10^{10} = 0.316$ , implying that 68.4% of the surface was covered by alumina. If the pore arrangement was exactly hexagonal in the whole film, the porosity would

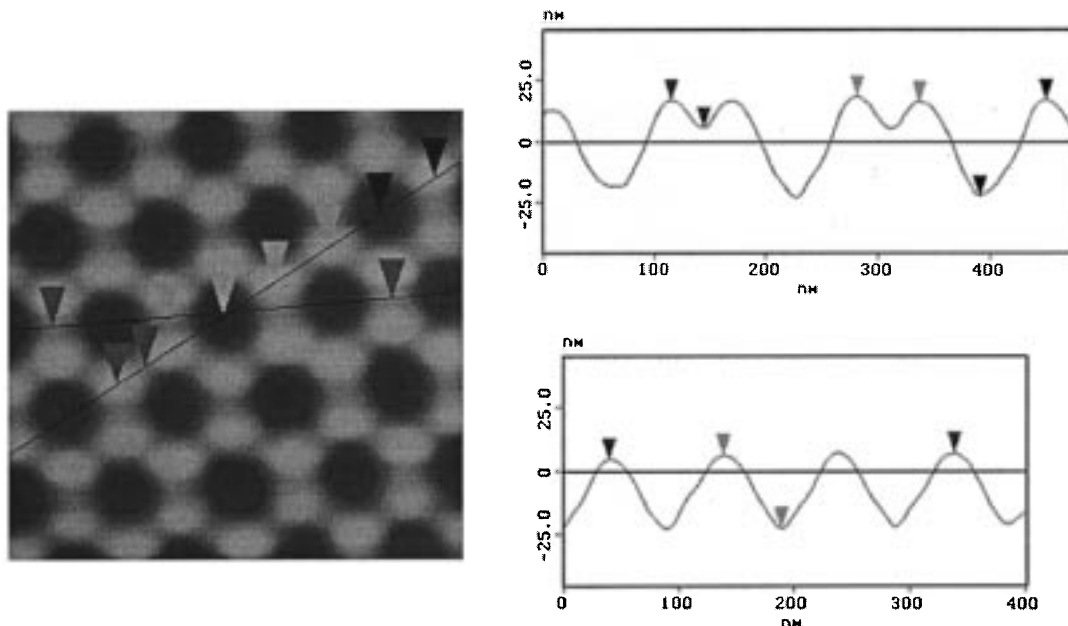


**Figure 13.** Cross-section AFM analysis of scallops within a domain: (left) enlarged detail of the AFM of Figure 12b; (top right) height profile through the tops of the barrier oxide “bumps” and the bottoms of the pores, corresponding to the diagonal line on left; (bottom right) height profile through the “passes” between the “bumps” of oxide and the bottom of the pores, corresponding to the almost horizontal line on left.

be  $r = \pi/3.464 \times (D_p/D_c)^2 = 0.302$ , and the electrochemical yield was  $100 \times (1 - 0.302) = 69.8\%$ . Both results were very close to the electrogravimetric estimate of 69.73% for anhydrous  $\text{Al}_2\text{O}_3$ .

The 30–31% loss of Al to the acidic solution is important, because if all Al atoms were converted to  $\text{Al}_2\text{O}_3$ , there would be a 70% increase of volume. The theoretical Pilling–Bedworth ratio (PBR)<sup>39</sup> is  $[(26.98 + 3.0 \times 15.994) \text{ g}/2 \times 3.0 \text{ g cm}^{-3}] / [26.98 \text{ g}/2.7 \text{ g cm}^{-3}] = 1.70$  for  $\text{Al} \rightarrow \text{Al}_2\text{O}_3$ ; such a large ratio implies large stresses and buckling of the interfacial region. If 31% of the Al is lost to solution, however, the effective PBR becomes  $1.70 \times 0.69 = 1.18$ . Lower values, closer to 1.0, have been measured elsewhere.<sup>28</sup>

**3.6. Local Temperature Increase.** That temperature increases during anodization can be proved by measuring a  $j-t$  anodizing curve while the stirring of the electrolyte is stopped and then restarted (Figure 14). If the reaction heat cannot be dispersed, then the temperature must increase and accelerate either chemical dissolution or oxide formation. Indeed, when stirring was stopped, the current density increased (Figure 14) and then resumed its previous value when stirring was restarted. Increasing the bath temperature increases the current density, as seen in Figure 15.

**3.7. Anodization at High Voltages.** The reaction rate was strongly affected by the voltage (Figure 16). The current density increased exponentially with the voltage; at 60 V the current density showed large fluctuations. After anodizing at 60 V and stripping the oxide, the Al surface was found to be very rough.

At high voltages, the chemical dissolution rate at the oxide/solution interface increases, as does Joule heating. Local temperatures may rise at the pore bottoms and stresses and rates of heat dissipation may become nonuniform, thus causing fluctuations in the anodizing current.

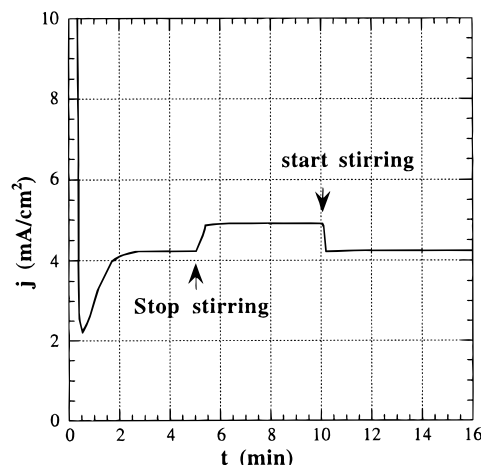


**Figure 14.** The effect of stirring on the current density at 40 V in 3%  $\text{H}_2\text{C}_2\text{O}_4$  at 15 °C.

**3.8. Stresses in Pore Growth.** Stresses (compressive and tensile) in oxide films have been widely discussed, particularly for BTF.<sup>2,40,41</sup> From strain measurements, for an Al sample with an oxide grown in 0.1 M  $\text{H}_2\text{SO}_4$  at  $<0.5 \text{ mA cm}^{-2}$ , the oxide is under compressive stress, while at higher current densities ( $3.5\text{--}5.3 \text{ mA cm}^{-2}$ ) there is a large tensile stress.<sup>40</sup>

**3.9. Temperature Rise in Pore Growth.** A local heating effect for pore growth, first proposed by Keller et al.,<sup>26</sup> has been ignored for a long time, because the temperature rise at the anode is not very high (5–25 °C). But this measured temperature rise may not represent the real local temperature at the bottoms of the pores; a large local heating, due to Joule heating and local oxide dissolution, could raise the temperature and introduce a large thermal stress in the barrier layer and at the metal/oxide interface.

(39) Pilling, N. B.; Bedworth, R. E. *J. Inst. Metals* **1923**, 29, 529.

(40) Nelson, J. C.; Oriani, R. A. *Corrosion Sci.* **1993**, 34, 307.

(41) Young, L. *J. Electrochem. Soc.* **1963**, 110, 589.

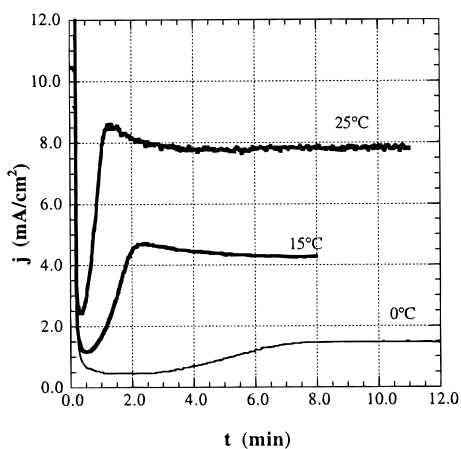


**Figure 15.** The effect of the bath temperature on the current density at 40 V in 3% H<sub>2</sub>C<sub>2</sub>O<sub>4</sub>.

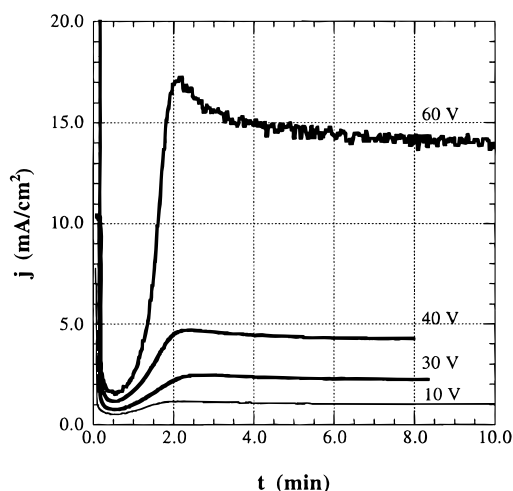


**Figure 16.** The effect of voltage on the current density in 3% H<sub>2</sub>C<sub>2</sub>O<sub>4</sub> at 15 °C.

An elementary one-dimensional calculation<sup>22</sup> of the possible heat rise at the bottom of the pores of PTF assumes that the electrical current concentrates at the pore bottom. Joule heating, due to electrical power dissipation within the high-resistance barrier oxide layer, is much larger than the exothermicity of the chemical reactions.<sup>42</sup> Using a Laplace transform and a numerical method, to integrate the equation for thermal conductivity in a semi-infinite region of the electrolyte, the calculated temperature change is  $\Delta\theta = 1.823/p[0.2629 + 3.07(\lambda C_p)^{1/2}]$ ,<sup>22,43</sup> where  $p$  is the porosity,  $\lambda$  is the thermal conductivity of the oxide, and  $C_p$  is its heat capacity. The estimated temperature rise within the electrolyte for the first 12 s, at bottom of the pore, is  $\Delta\theta(\text{calc}) = 21$  °C.<sup>22</sup> This result disagrees with a previous steady-state calculation of  $\Delta\theta(\text{calc}) = 0.06$  °C,<sup>42</sup> but agrees with an experimental temperature rise of the anode temperature of  $\Delta\theta(\text{exp}) = 25$  °C.<sup>44</sup>

#### 4. Phenomenological Theories of Pore Formation

Before presenting our own suggestions for a possible mechanism of pore formation in section 7, we review in

sections 4 and 5 what has been proposed in the literature; in section 6 we compare and contrast barrier type films and pore-type films, because some insight into a mechanism for PTF may be found here. In section 7 we gather tentative conclusions, some buttressed by our own observations, about pore-type films.

Early theories of porous oxide formation were reviewed,<sup>4</sup> with a thought that “theorists have been slow in explaining how or why the quite remarkable uniform spatial distribution of pores came about in the first place, nor why it is so specifically related to the formation voltage”.<sup>4</sup>

The ranges of pore diameters and cell diameters in PTF are much larger than any crystallographic periodicity or any reasonable supercell size for either Al or any of its oxides; therefore, it is clear that the formation of alumite is not a crystal growth phenomenon. Regular arrays of cells (lamellar and rod eutectics, e.g. pearlite) can also form during the solidification of liquids,<sup>45–47</sup> but these structures have 10 mm scales; therefore it is also clear that liquid–solid instabilities will not explain PTF either.

Marangoni ordering may occur in the solution above the pores.<sup>48,49</sup> [The Marangoni effect is an interfacial surface tension effect between two liquids (which explains<sup>48</sup> the old Bénard problem<sup>50–52</sup>). It is not known whether a Marangoni mechanism is operative in PTF formation. Once the pores form, their evolution can be modeled by Monte Carlo techniques (Voronoi diagrams),<sup>53,54</sup> but this sheds no light on why or how the pores form.

It has been suggested that, at the bottom of the pores, the pH drops precipitously, increasing the solubility of the oxide; this is an “autocatalytic mechanism of pit propagation”.<sup>6,55,56</sup> There may be a pronounced temperature and concentration differential between the pore base and the bulk electrolyte.<sup>4,44</sup> The cracks on the surface of the air-formed oxide layer can also be centers for pore nucleation,<sup>34</sup> but they are unlikely to be a major factor, because of their low density.

Thompson and Wood<sup>3</sup> assumed the following mechanistic sequence: (1) electropolishing or other pretreatment left a slightly scalloped surface of aluminum covered by oxide; (2) a scalloped “native” barrier oxide film grew over this scalloped surface; (3) as anodization started, pores would start at cracks and imperfections in the surface, leaving an electric field concentrated below the regions where the oxide film was thinner, thus (4) aiding the local dissolution of oxide; (5) this new pore

(45) Pelcé, P., Ed. *Dynamics of Curved Fronts*; Academic: New York, 1988.

(46) Zener, C. *AIME Trans.* **1946**, 167, 550.

(47) R. H. Brandt, *J. Appl. Phys.* **1945**, 16, 139.

(48) Pearson, J. R. A. *J. Fluid Mech.* **1958**, 4, 489.

(49) Nield, D. A. *J. Fluid Mech.* **1964**, 19, 341.

(50) Bénard, H. *J. Phys.* **1900**, 9, 513.

(51) Lord Rayleigh *Philos. Mag.* **1916**, 32, 529.

(52) Chandrasekhar, S. *Hydrodynamic and Hydromagnetic Stability*; Clarendon Press: Oxford, 1961.

(53) Randon, J.; Mardilovich, P. P.; Govyadinov, A. N.; Paterson, R. *J. Colloid Interface Sci.* **1995**, 169, 335.

(54) Anis, D.; Bhattacharya, B. K. *Adv. Computing Res.* **1983**, 1, 159.

(55) Hoar, T. P. *Electrode Processes*; Butterworths: London, 1961; p 299.

(56) Vetter, K. J.; Strehblow, H. H. In *Localized Corrosion*; Staehle, R. W., Brown, B. F., Kruger, J., Agrawal, A., Eds.; National Assoc. Cor. Engrg: Houston, 1974; p 240.

(42) Nagayama, M.; Tamura, K. *Electrochim. Acta* **1968**, 13, 1773.

(43) Carslaw, H. S.; Jaeger, J. C. *Conduction of Heat in Solids*; Clarendon Press: Oxford, 1959; p 76, eq 9.

(44) Mason, R. B. *J. Electrochem. Soc.* **1955**, 102, 671.

bottom deepened, and a "major" pore formed, at the expense of the former shallow pores.<sup>3</sup> At the metal/oxide interface the average field across the barrier layer determined the barrier film growth rate, while at the oxide/electrolyte interface the local field at the pore bottom, assisted by local heating, determined the oxide dissolution rate.<sup>3</sup> The film growth rate was approximately constant and independent of pore bottom curvature, while the dissolution rate increased as the pore base radius of curvature decreased. As the pore radius of curvature decreased, the film dissolution rate increased, to enlarge the pores; if the pore radius became too big, the dissolution slowed and the pores tended to fill; these two competing processes kept the pore radius constant.<sup>3</sup>

### 5. Mathematical Theories of Pore Formation

Parkhutik and Shershulsky presented a kinetic theory for single-pore growth.<sup>33</sup> They assumed that the electric field in the scalloped barrier oxide at the bases of each pore was inhomogeneous both laterally (i.e. along the oxide surface) and also inwardly (i.e. within the oxide layer) and that the depth dependence of  $E$  was due mostly to the nonplanarity of the interfaces.<sup>33</sup> By assuming a hemispherical pore bottom, they found that the pore radius,  $R_m$ , is a function of the applied potential,  $U_0$ ,<sup>33</sup>

$$R_m = -U_0/E_{eo}(1 - k) \ln(1 - k) \quad (2)$$

where  $k$  is a function of oxide formation and oxide dissolution rate constants  $k_{ox}$  and  $k_{diss}$  and of three parameters,  $\alpha$ ,  $\beta$ , and  $\gamma$ ,

$$k = 1 - [(\beta/\gamma)(k_{ox}/k_{diss} - 1)/(1 + \beta k_{ox}/\alpha k_{diss})]^{1/2} \quad (3)$$

and that  $R_m$  is also a function of pH

$$R_m = R_{mo}/\{1 - 2.3\eta \text{ pH} [\ln(\alpha A_0 k_{diss}/\beta B k_{diss})]^{-1}\} \quad (4)$$

where  $R_{mo}$  is the pore radius extrapolated to pH 0.<sup>33</sup> These equations<sup>33</sup> for  $R_m$  reproduced the experimental<sup>57</sup> linear dependence of the pore radius  $R_m$  on voltage  $U_0$  and also the experimental<sup>57</sup> quasilinear dependence of pore radius  $R_m$  on pH. This theory maintained the assumed initial hemispherical shape for a pore bottom<sup>33</sup> but did not explain how this shape started, nor did it explain the hexagonal ordering of the pores.

A theoretical effort attempted to prove the curved growth front in porous Si.<sup>58</sup>

A recent theory of pattern formation during electropolishing of aluminum<sup>10,37,59</sup> proposed that the curved barrier oxide forms because molecules of ethanol (the majority constituent of a commercial electropolishing solution) adhere preferentially along the "ridges" of the oxide, rather than on the pore bottoms; this adhesion would facilitate increased corrosion at the relatively more exposed pore bottoms.<sup>10,37</sup>

Pore growth involves heating.<sup>44,60</sup> Temperature increases between 1 and 25 K have been measured;<sup>3</sup> a

calculation estimated that 84% of the heat is produced by local Joule heating but predicted only a small temperature rise (<1 K) in the electrolyte at steady state.<sup>42</sup> A large temperature rise (25 K) was calculated at the pore bottom in the absence of convection.<sup>22</sup>

### 6. Comparison of Growth of PTF and BTF

A successful theory for organized pore growth of alumite should start from the salient differences between Al anodization in basic or at neutral pH (BTF, where no pores grow, although they may form), and anodization at acidic pH (PTF, where pores form and grow efficiently).

(1) For BTF, the Faradaic current efficiency in building oxide is high (close to 100%); the metal/oxide and oxide/solution interfaces remain planar; the current decays exponentially with time; some pores may form at the oxide/electrolyte interface, but do not grow. For PTF, the Faradaic efficiency in making oxide is lower (70% or below); both the metal/oxide and oxide/solution interfaces become curved (spherical segments); the current rises dramatically, until a steady-state current is reached. The barrier oxide layer continuously regenerates at the pore bottoms but retains a small but constant thickness. The pore walls consist of amorphous  $\text{Al}_2\text{O}_3$ , some conjugate anions of the forming acids (up to 20%), small amounts of water, and some nanocrystallites. The pore diameter is uniform; the pore height increases linearly with time.

(2) The large overpotential in the formation of PTF (about 10–150 V) may generate highly localized Joule heating at the oxide/electrolyte interface. The barrier layer at the bottom of the pores in PTF is a dielectric, with a large potential drop across it. The local electric field is on the order of  $\text{MV cm}^{-1}$ . In BTF about 10% of the ions may be mobile.<sup>8</sup>

(3) In PTF Joule heating, the overvoltage and the high current density at the oxide/electrolyte interface, together with the exothermic acid-catalyzed alumina dissolution, may raise the local temperature. The increase in anode temperature was measured by several authors<sup>44,60</sup> and estimated to be small by a calculation of the steady-state temperature in the electrolyte;<sup>42</sup> a larger temperature rise is estimated in the absence of convection.<sup>22</sup>

(4) For PTF growth at the bottom of the pores,  $\text{Al}^{3+}$  ions migrate from the metal across the metal/oxide boundary into the barrier oxide;  $\text{O}^{2-}$  ions are formed as  $\text{O}^{2-}$  (oxide) from water at the oxide/electrolyte boundary and migrate into the barrier layer. Roughly 30% of the  $\text{Al}^{3+}$  ions in the oxide dissolve into the electrolyte, with an additional release of local heat: this dissolution is acid-catalyzed. The two sources of the protons required for this dissolution are the bulk electrolyte (but these protons must move against the applied potential) and the protons liberated when water splits at the oxide/electrolyte surface to produce  $\text{O}^{2-}$  (oxide).

(5) In PTF, the volume change, due to oxide formation and to thermal expansion, may introduce stresses within the barrier layer.

(6) In PTF (but not in BTF), a curved metal/oxide interface is somehow formed; a similar curved interface forms at the oxide/electrolyte interface.

(57) Ebihara, K.; Takahashi, H.; Nagayama, M. *J. Met. Finish. Soc. Jpn.* **1982**, *33*, 4.

(58) Zhang, X. G. *J. Electrochem. Soc.* **1991**, *138*, 3750.

(59) Yue, D.-F., Ph.D. Dissertation, Notre Dame University, 1995.

(60) Applewhite, F. R.; Leach, J. S.; Neufeld, P. *Corros. Sci.* **1969**, *9*, 305.

(7) In PTF, a hexagonal ordering of both the pores and of the pillars made of amorphous Al<sub>2</sub>O<sub>3</sub> sets in initially at critical times and voltages of electropolishing<sup>10,37</sup> or can be induced by long-term anodizing,<sup>21,24</sup> by repetitive anodization/stripping cycles, or by nanoindentation with a SiC template at the “right” spacings.<sup>36</sup>

## 7. Proposed Mechanism of Pore Formation

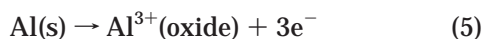
We now provide, in 15 points, a possible mechanism for pore formation. Points 1–8 are relatively self-evident suggestions based on the overall chemistry. Points 9–15 are insights or conclusions based on our own results.

During PTF formation, hydrogen ions and the electric field at the oxide/electrolyte interface must play important roles.

(1) Electropolishing flattens some large surface irregularities, but also creates<sup>62</sup> a large number of small pores (Figure 3a). Figure 3a shows pit sizes from a few to tens of nanometers and a pit density of about 10<sup>10</sup>–10<sup>12</sup> pits cm<sup>-2</sup>. Some of these pits can develop into pore nuclei. Their density will decrease as pores grow, because pores merge as anodizing time increases.

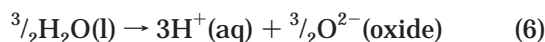
The thickness of an air-formed oxide layer may be small but nonuniform, supporting a huge electric field gradient (several MV cm<sup>-1</sup>) across it. In PTF, the electric field and the ionic current density should be larger at the pore bottoms than between the pores.<sup>3</sup>

(2) For both PTF and BTF, Al<sup>3+</sup> ions form at the metal/oxide interface



and migrate into the oxide layer.

(3) For both BTF and PTF, at the oxide/electrolyte interface the water-splitting reaction

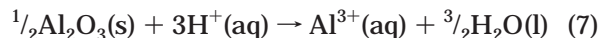


occurs and is rate-determining.<sup>6,61</sup> The O<sup>2-</sup>(oxide) ions migrate, thanks to the electric field, within the oxide from the oxide/solution interface toward the metal/oxide interface, to form Al<sub>2</sub>O<sub>3</sub>. The oxide formation rate constant *k*<sub>ox</sub> of ref 33 must be the rate for eq 5 or 6, whichever is slower.

(4) In BTF, and particularly in base, the protons or hydronium ions generated by the water-splitting reaction are neutralized locally by the reaction

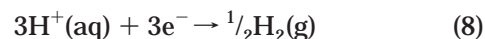


(5) In contrast, in PTF the protons can locally dissolve more oxide:



The oxide dissolution rate constant *k*<sub>diss</sub> of ref 33 must be the rate for eq 7. In section 3.5 we measured that about 30% of the current produced dissolved species, while 70% of the current produced solid oxide.

(6) Hydronium ions can also migrate toward the cathode, where they leave the electrolysis cell as H<sub>2</sub> gas, completing the circuit:



(7) By charge balance in PTF and BTF, the rates of eqs 5 and 8 must be equal.

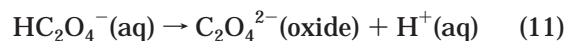
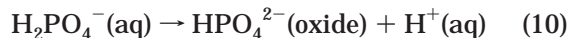
(8) Much of the oxide produced by eq 6 constructs the “sidewalls” of the PTF. In a PTF eq 7 will be slower than eq 5. The water-splitting reaction (eq 6) will thicken both BTF and PTF barrier films.

The main difference between BTF and PTF is eq 7, which must occur preferentially at the pore bottom and keep the PTF barrier oxide thin. The absence of eq 7 makes the BTF uniform.<sup>62</sup> For PTF, eq 7 must occur preferentially where the electric field is highest, i.e., at the center or close to the center of the pore bottom.

We now present points 9–15 that are a new contribution of this study.

(9) The growth of the porous anodic oxide (“sidewalls”) in PTF must now be explained. Since, as seen in Figure 8, the pore walls are uniform through their length, the key growth step must be near the pore bottom, probably very close to the circle of intersection between the cylinder of the pore wall and the spherical segment of the pore bottom. At this circle of intersection the water-splitting reaction (eq 6) must also occur, but eq 7 should not occur. Thus the porous oxide can grow, fed by Al<sup>3+</sup> ions from “below”, and from O<sup>2-</sup>(oxide) ions from “the side”. Figure 13 seems to show that the pore thickness is not circularly symmetric around the pore bottom, but this is probably an artifact. The dissolution of the pores by phosphoric acid–chromic acid exposes the barrier oxide, which has “lumps” because its growth is greatest in the region farthest from three adjacent pores. This is quite obvious from the AFM profiles of Figure 13.

(10) At these sides of the bottom of the pores, there is probably some competition between the water-splitting reaction (eq 6) and the dissociation of acids to form conjugate base anions,



so that the conjugate base anions can replace O<sup>2-</sup> in the oxide, as substitution or contamination impurities within some depth, as seen by the UMIST group.<sup>3,34</sup> Chromic acid does not have a protonated conjugate base and thus does not incorporate into the pore walls.<sup>3</sup> The importance of eqs 9–11 has not, to our knowledge, been emphasized before: we can now explain for the first time why dichromate does not incorporate into the pore walls.

(11) Both BTF and PTF usually start from some Al surface that is fairly smooth (hills of at least 3 nm height), but with pits formed at lattice imperfections or by electropolishing (i.e. etching or “preanodization”). These Al pits will be covered by an air-formed oxide, so that both the metal/oxide and the oxide/electrolyte interfaces are locally curved. The oxide thickness may

(61) Valand, T.; Heusler, K. E. *J. Electroanal. Chem.* **1983**, *149*, 71.

(62) Shimizu, K.; Kobayashi, K.; Skeldon, P.; Thompson, G. E.; Wood, G. C. *Corrosion Sci.* **1997**, *39*, 701.

be uniform or irregular; its coverage of the Al metal surface is neither perfect nor complete. This is an obvious conclusion from the observation that aluminum is macroscopically conductive despite the oxide coverage.

(12) As anodization starts, the electric field at the oxide/electrolyte interface should be greater at sites where the native oxide coverage is thinner, or else the metal/oxide interface flattens out initially, so that the oxide layer is thicker in some parts of the surface, allowing the electric field to concentrate where the oxide is thinner. We do not yet have experimental data that can discriminate between these two possibilities. In BTF, any local electric field increase does not encounter acid-catalyzed oxide dissolution, and pores do not grow.

(13) In PTF, as pore growth continues, a curved metal/oxide interface is maintained or reestablished at the pore bottom, to match the curved oxide/electrolyte interface. This constant thickness of the barrier oxide layer was well-established in previous studies, can be seen vaguely in Figure 8, and is very clear in more recent cross-sectional TEM micrographs (to be published later).

(14) Once small pores have formed, the acid and electric potential penetrate into the pore, and the growth becomes self-catalyzing.<sup>33</sup>

(15) If the pores are not ordered, then a horizontal mobility of ions in the barrier layer<sup>8</sup> allows for a reordering of the pores, until an equilibrium hexagonal ordering is reached. This is a potentially significant new conclusion of the present study.

## 8. Discussion

Nanopores in aluminum oxidized in strong acids can become ordered either at certain voltages and times of the initial electropolishing<sup>10</sup> or by long-term anodization and reanodization,<sup>24</sup> by nanoindenting at the "right" positions then anodizing,<sup>36</sup> or by the multiple reanodization demonstrated above. Ordered pore domains

grow linearly with time and increase with increasing temperature. Significant heating occurs during pore growth.

We suggest that the pores are initiated when the electric field is increased into a shallow pore bottom and initiates local acid corrosion. The pore walls are generated in a circular ring around the bottom, with occasional incorporation of conjugate base anions into the pore walls. The hexagonal ordering occurs either (i) by an evolutionary selection of those pore bottoms that have the correct spacing<sup>33</sup> for the acid and voltage used or (ii) by a diffusion of the pore bottoms, aided by lateral mobility of the ions that constitute the barrier layer.

## 9. Conclusion

The following are the main conclusions of this study.

(1) Domain structures form in hexagonally ordered anodic alumina films; the average domain sizes are a linear function of time. The domains form by pores moving and/or merging.

(2) Pore nucleation in PTF occurs as the barrier layer is first formed, concentrates where the oxide is thinnest, and involves an acid-catalyzed partial oxide dissolution in PTF at the pore bottoms, where the electric field is highest. This acid-catalyzed process is absent in BTF.

(3) Joule heating and acid-catalyzed oxide dissolution heat the pore bottom.

(4) The hexagonal ordering of the pores is not yet explained, but the mobility of ions within the barrier oxide<sup>8</sup> and of Al atoms within the metal may explain why pores can rearrange dynamically and why linear domain growth with time is possible.

**Acknowledgment.** This work was supported by DOD-USARO-DAA-H04-96-1-0316. We are grateful to Prof. William D. Doyle for his support, constructive criticism, and encouragement.

CM980163A